Catalysis Letters (2020) 150:2487–2496
https://doi.org/10.1007/s10562-020-03156-5

Sulfur Doped Carbon-Rich g-C_3N_4 for Enhanced Photocatalytic H_2 Evolution: Morphology and Crystallinity Effect

Dan Long[1] · Lu Wang[1] · Hongyue Cai[1] · Xi Rao[1] · Yongping Zhang[1]

Received: 23 December 2019 / Accepted: 20 February 2020 / Published online: 12 March 2020

Abstract

Molecular design for the intercalation of S and C in the framework of g-C_3N_4 is a promising strategy to increase visible light harvesting and facilitate the separation of photoinduced electron/hole pairs. Herein, we reported a facial method to prepare porous S doped g-C_3N_4 nanotubes by thermal polymerization of urea and 2-thiobarbituric acid. The obtained catalysts contain certain carbon and sulfur atoms in the aromatic rings substituting the nitrogen atoms in g-C_3N_4, which narrows down the band gap, and increases the separation of photoinduced charge carriers. Meanwhile, nanotube formation increases the specific surface area of catalyst. The synergistic effect of S doped carbon rich g-C_3N_4 and nanostructure forming results in superior photocatalytic H_2 evolution from water splitting. The study shows that the photocatalytic H_2 evolution is correlated with the crystallinity of S doped g-C_3N_4.

Graphic Abstract

Schematic illustration for framework of 0.3S-CN and its photocatalytic hydrogen evolution mechanism.

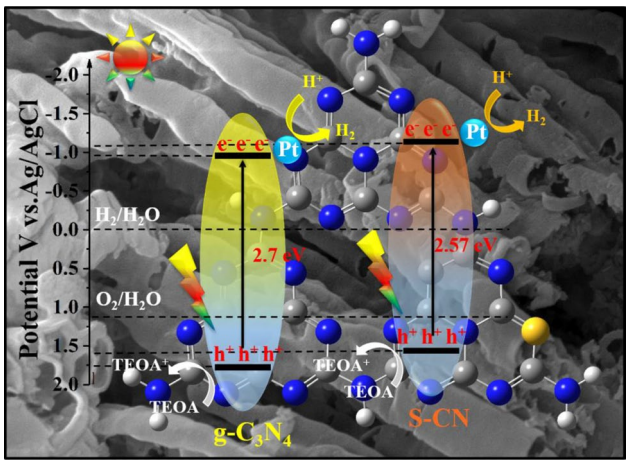

Keywords Graphitic carbon nitride · Element doping · Sulfur · Photocatalytic hydrogen evolution

1 Introduction

Photocatalysis technology is considered as one of the most promising ways to achieve sustainable energy production and environmental restoration since it can effectively convert solar energy into chemical energy and degrade organic pollutant under solar light irradiation [1–7]. Graphitic carbon nitride (g-C_3N_4), as a non-metallic organic semiconductor

Electronic supplementary material The online version of this article (https://doi.org/10.1007/s10562-020-03156-5) contains supplementary material, which is available to authorized users.

✉ Xi Rao
raoxiemail@swu.edu.cn

✉ Yongping Zhang
zhangyyping@yahoo.com

[1] School of Materials and Energy, Southwest University, Chongqing 400715, China

material with a two-dimensional layered structure, is considered to be a very promising visible photocatalyst because of its good chemical stability, narrow band gap energy, simple preparation technique and low cost [8–12]. However, the low hybridization between atoms results in its response only in the ultraviolet light region, and the absorption of visible light is insufficient, which greatly reduces the photocatalytic efficiency of g-C_3N_4 [13]. The photocatalytic quantum efficiency of g-C_3N_4 still needs to be improved to achieve large-scale industrial applications. Thus, many methods have been proposed to improve the photocatalytic activity, such as element doping [14–17], size and morphology designing [18–21], porosity forming [22, 23], metal cluster supported on carbon nitride [24–26], composite with other semiconductor materials to form heterojunction [27–29].

Generally, it is an effective strategy to modify the electronic structure of semiconductors and their surface properties by using the element doping, which can effectively improve their photocatalytic performance. Recently, for g-C_3N_4 and other conventional photocatalysts (such as TiO_2) [30], it has been proved that the element doping strategy (such as doping anionic elements such as B, P or F) can effectively improve the photocatalytic efficiency [31–34]. Zhang et al. showed that the photocatalytic activity of g-C_3N_4 was increased by P doping [35]. Dong et al. verified that the nonlocal large π bond formed by the homo-doping of carbon in g-C_3N_4 can cause the change of intrinsic electron and band structure, thus improving the absorption of visible light, and the specific surface area and photocatalytic efficiency [16]. The electronic structure changes after sulfur replaced nitrogen in g-C_3N_4 by first principle calculation, and the band gap of the doped material became narrowed [13]. However, these studies have shown that sulfur doped graphite carbon nitride can effectively improve the photocatalytic efficiency of g-C_3N_4 in the degradation of dyes, but there are few reports on the enhancement of visible light hydrogen evolution [36–38].

Herein, we report a facile route to prepare S doped carbon rich g-C_3N_4 for hetero- and homo-elements doping by polymerizing 2-thiobarbituric acid and urea. During pyrolysis process, sulfur and carbon atoms were intercalated in the six-membered conjugated rings by a hydrothermal method (scheme 1). The unique electronic structure of sulfur doped carbon rich g-C_3N_4 enhances the visible light harvesting and facilitates the transport and separation of photoinduced charge carriers.

2 Experimental Details

2.1 Synthesis of the S Doped g-C_3N_4 Microtubes

All chemicals were of analytical grade and used as received without further purification. First, 10 g urea was dissolve in the solution of 5 mL absolute ethanol and 5 mL water under magnetic stirring for 10 min. Different amount of 2-thiobarbituric acid (0.005 g, 0.01 g, 0.03 g, 0.05 g and 0.1 g) was dissolved in the urea solution under magnetic stirring for 10 min, and then the solution was dried in oven at 60 °C. The white powder was heated at 550 °C for 2 h with a heating rate of 3 °C/min at N_2 atmosphere. The obtained yellow powder was labeled as 0.05S-CN, 0.1S-CN, 0.3S-CN, 0.5S-CN and 1S-CN, corresponding to samples with the ratio of 2-thiobarbituric acid to urea is 0.05 wt%, 0.1 wt%, 0.3 wt%, 0.5 wt%, and 1 wt%, respectively. The reference sample was prepared by the same method with 10 g urea and labeled as CN.

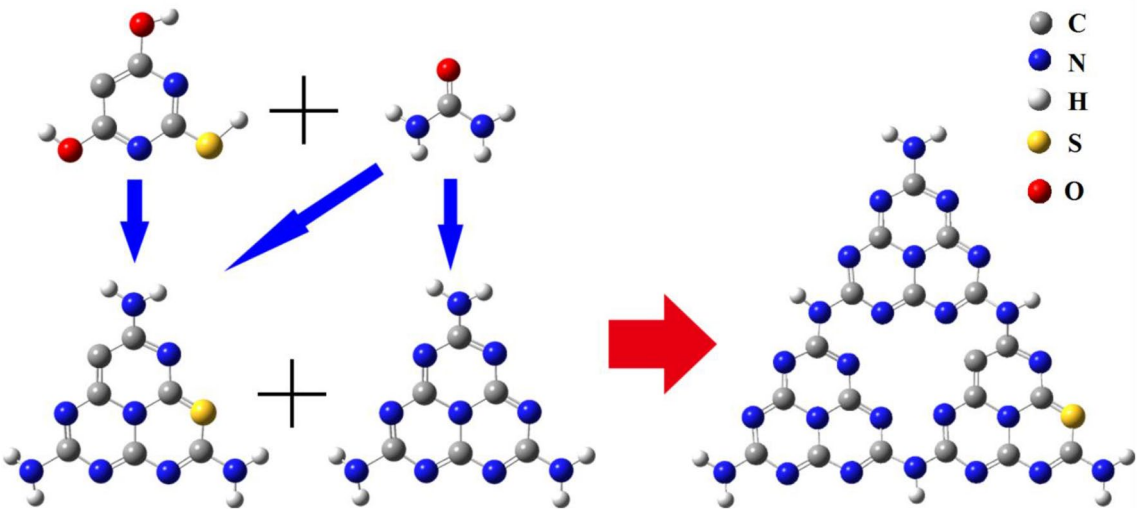

Scheme 1 Molecular design strategy for forming the sulfur doped g-C_3N_4 using urea as precursor and 2-thiobarbituric acid as S source

2.2 Characterization

The morphology was observed by a scanning electron microscope (SEM, JSE-7800F, Jeol) and a transmission electron microscope (TEM, Libra 200FE, Zeiss). The X-ray diffraction (XRD) patterns were recorded with a ShimadzuXRD7000 instrument using Cu Kα as the radiation source (λ = 1.5418 Å). Fourier transform infrared (FTIR, Frontier) experiments were carried out using a Perkin Elmer spectroscopy instrument in KBr pellets. X-ray photoelectron spectroscopy (XPS) was carried out to analyze the chemical state and composition on a VG ESCALAB 250 spectrometer with Al Kα radiation (hν = 1486.8 eV). Ultraviolet–visible (UV–vis) diffusion reflectance spectra were performed on U-3310 spectrophotometer (Hitachi, Japan) in the wavelength range of 300 to 800 nm. Photoluminescence (PL) measurements were carried out on a F-7000 fluorescence spectrophotometer (Hitachi, Japan) with an excitation wavelength at 273 nm using a 150 W Xe lamp as the excitation source. The nitrogen adsorption–desorption isotherms and the Brunauer–Emmett–Teller (BET) specific surface areas were measured at − 196 °C on an ASAP-2010 apparatus. The total pore volumes were estimated from the adsorbed amount of N_2 at a relative pressure P/P_0 of 0.995. Transient photocurrent and electrochemical impedance spectroscopy (EIS) measurements were conducted on an Autolab electrochemical workstation (PGSTAT302N) in a standard three-electrode system, using a platinum wire and the saturated Ag/AgCl electrode as the counter electrode and reference electrode, respectively. 0.25 M Na_2SO_4 aqueous solution was used as electrolyte. The working electrode was prepared by coating the catalysts on a 1.8 cm × 1.2 cm fluorine-doped tin oxide (FTO) glass substrate. A 500 W Xe lamp with a 420 nm cutoff filter (λ > 420 nm) and a light intensity of 113.8 mW/cm^{2}was used as a light source. Mott-Schottky plots were taken at a frequency of 1000 Hz with a bias potential that ranged from 1.0 to − 1.0 V (vs Ag/AgCl).

2.3 Photocatalytic Hydrogen Generation

Photocatalytic performance was carried out by a full spectrum photocatalysts performance evaluation system (Suncat Instruments Co. China). The reactor was made up a quartz container with highly transparent window in a diameter of 2.5 cm at the bottom. The irradiation light source was a 500 W Xe lamp (Zolix, Gloria-X500A) with a 420 nm cutoff filter (λ > 420 nm). The reactor with volume of 130 mL was kept at 20 °C and the light intensity was 113.8 mW/cm^2. 10 mg of photocatalyst was dispersed in 30 mL water solution with 17% volume concentration triethanolamine (TEOA) as the sacrificial electron donor, while 1 wt% Pt ion ($H_2PtCl_6 \cdot H_2O$) was loaded on the surface of the samples by an in situ photodeposition method. Prior to irradiation, the reactor was evacuated to high vacuum up to 10^{-8} Torr to remove air and filled with argon. The reaction suspension was stirred with a magnetic stirrer under irradiation. During the photocatalytic process, 1 mL of the gas sample was withdrawn from the reaction cell at 30 min intervals and the pressure was automatically compensated with argon. The amount of hydrogen evolved was measured per 30 min with online Shimadzu gas chromatography (GC-2018; Molecular sieve TDX-01, Ar carrier gas) using a thermal conductivity detector (TCD). The apparent quantum yield (AQY) of the photocatalysts was calculated according to the light absorption and H_2 evolution rate as follows,

$$\mathrm{AQY}(\%) = \frac{\text{number of transfered electrons in reaction}}{\text{number of incident photons}} \times 100\% = \frac{2 \times \text{number of evolved } H_2 \text{ molecules}}{\int_{420}^{760} S \times I/E_\lambda} \times 100$$

where S is the irradiation area, I is the light intensity, and E_λ is the photon energy with wavelength of λ.

3 Results and Discussion

SEM and TEM reveal the morphology and microstructure of pure g-C_3N_4 and S-doped g-C_3N_4 with different ratio of 2-thiobarbituric acid. Figure 1a shows the CN image, appearing as a layered massive particle with flocculent lamellar structure. Figure 1b–f shows the SEM images of S-doped g-C_3N_4 with different amount of 2-thiobarbituric acid. The morphologies of catalysts appear as a loose tubular structure, and the surface of the tube is rough and irregular. With the increase of 2-thiobarbituric acid, the loose nanotube structure was gradually formed with the more dispersed flocculent lamellar structure. The nanotube structure is regular and complete for 0.3S-CN, as shown in Fig. 1d. With the 2-thiobarbituric acid amount more than that of 0.3S-CN, there appears more pores on the wall of nanotube. The TEM images, in Fig. 1g–h, show that some parts of the 0.3S-CN catalyst is lamellar structure, and some parts shows loose tubular structure, and there exists some fragments in the tube. The morphologies are similar to the porous nanotubes synthesized via thermal polymerization of urea [39]. The results showed that the introduction of 2-thiobarbituric acid affected the surface morphology of CN, increased the specific surface area and formed more active sites.

Figure 2a shows the XRD patterns of pure g-C_3N_4 and S-doped g-C_3N_4. All catalysts have two different diffraction peaks at about 13.1° and 27.5°, which are consistent with the characteristic (100) and (002) diffraction peaks of g-C_3N_4 (JCPDS 87–1526). After S-doping, the diffraction angle shifts from 27.25 to 27.35°, indicating that the spacing distance decreases due to the increased interaction

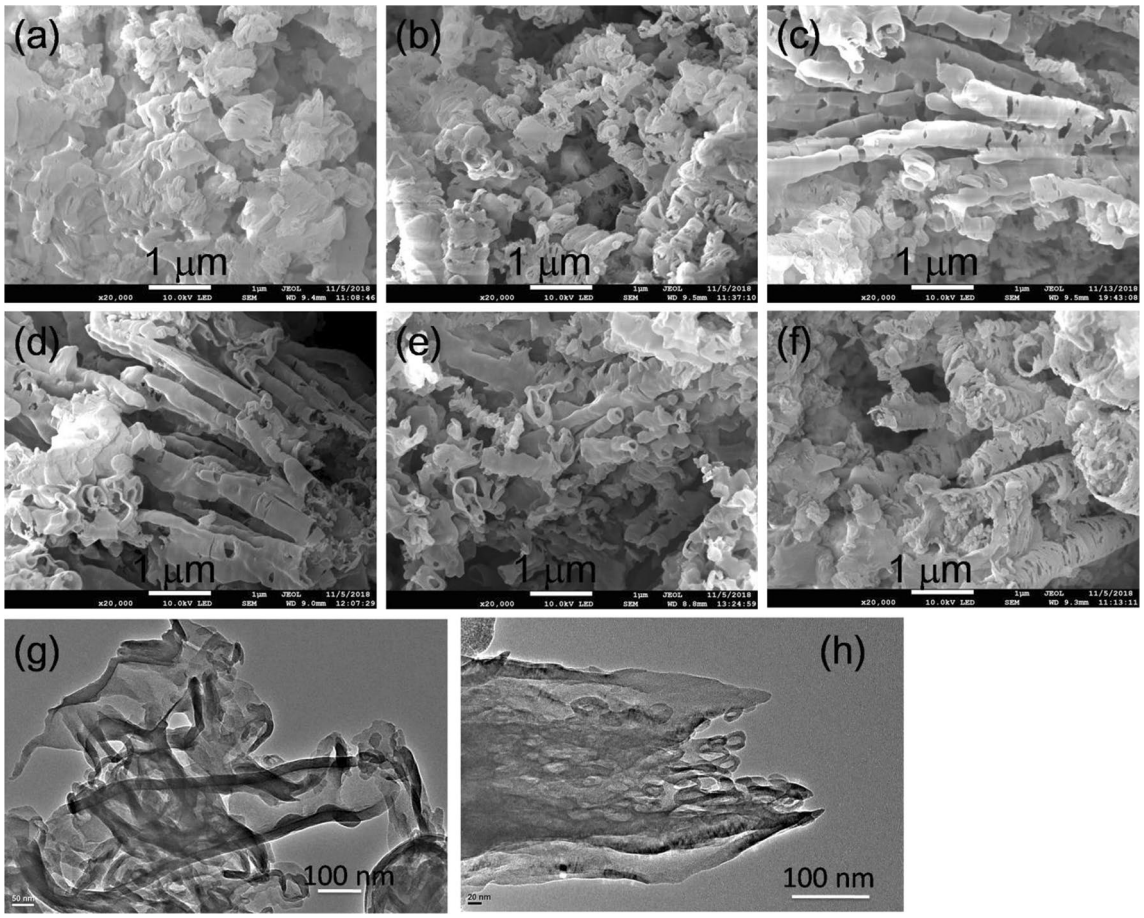

Fig. 1 SEM images of CN (**a**), 0.05S-CN (**b**), 0.1S-CN (**c**), 0.3S-CN (**d**), 0.5S-CN (**e**), and 1S-CN (**f**).TEM images of 0.3S-CN (**g**–**h**)

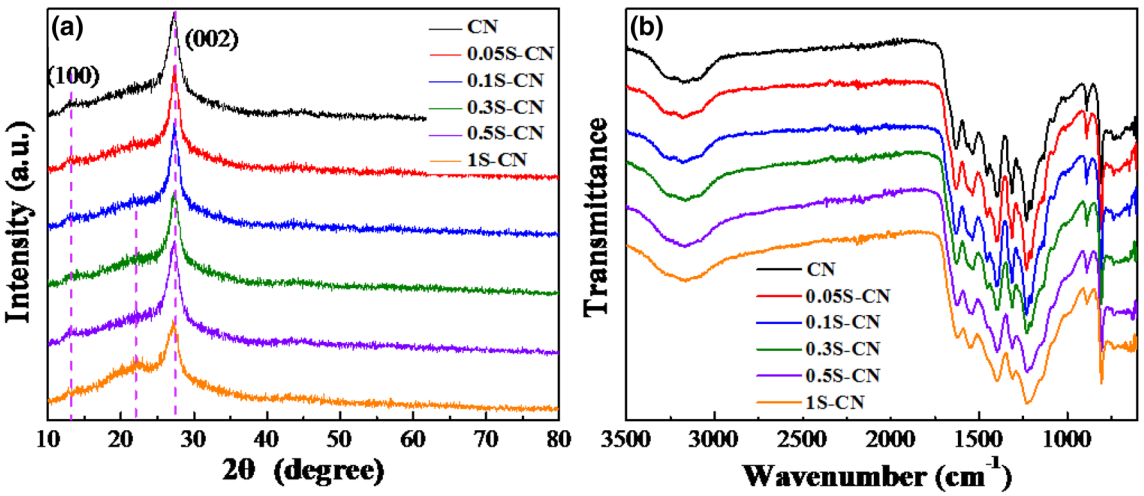

Fig. 2 XRD patterns (**a**) and FTIR spectra (**b**) of CN, 0.05S-CN, 0.1S-CN, 0.3S-CN, 0.5S-CN, and 1S-CN

between layers. When the amount of 2-thiobarbituric acid reaches 1 wt%, a diffraction peak appears at 21.9° caused by the introduction of 2-thiobarbituric acid. Detailed analysis (Figure S1) showed the crystallinity of S-doped g-C_3N_4 increases with 2-thiobarbituric acid at first, and 0.3S-CN has the highest crystallinity. Beyond that amount,

the crystallinity decreases with the increase of 2-thiobarbituric acid amount. Figure 2b shows the FT-IR spectra of CN, 0.05S-CN, 0.1S-CN, 0.3S-CN, 0.5S-CN and 1S-CN catalysts. The peak at 810 cm^{-1} is the bending vibration absorption of triazine structure. The peaks at 1233 cm^{-1}, 1315 cm^{-1}, 1400 cm^{-1}, 1460 cm^{-1}, 1540 cm^{-1} and 1643 cm^{-1} correspond the stretching vibration of aromatic ring. the peaks at 3000–3500 cm^{-1} are corresponding to the N–H stretching vibration of amino groups by incomplete condensation. The peaks remains at same position for different amount S doping. But the corresponding vibration peaks weakens slightly with the increase of S doping. This shows S doping does not change the skeleton structure of g-C_3N_4.

The measured N_2 adsorption–desorption isotherms are shown in Fig. 3a to characterize the specific surface area of the catalysts. The specific surface area of 0.3S-CN is 136.097 m^2/g, which is larger than 104.77 m^2/g of CN. The results show that formation 0.3S-CN nanotube increases the specific surface area dramatically, thus provide more active sites in the photocatalytic reaction [39]. The corresponding mesoporous distribution of the sample is shown in Fig. 3b. It can be seen that the mesoporous size is mainly distributed between 1–6 nm. The mesoporous surface of the material helps to increase the specific surface area of the material and enhance the photocatalytic activity.

Figure 4 shows the high-resolution XPS spectra of C, N, and S elements for CN, and 0.3S-CN nanotubes. The high-resolution C1s XPS spectra in Fig. 4a can be fitted into three peaks centered at 287.9 eV, 285.9 eV, and 284.4 eV, corresponding to the sp^2 hybrid C atoms bonded to N-containing aromatic skeleton rings (N–C=N) coordination, C–NH_2 bonded in the triazine ring, and the graphitic

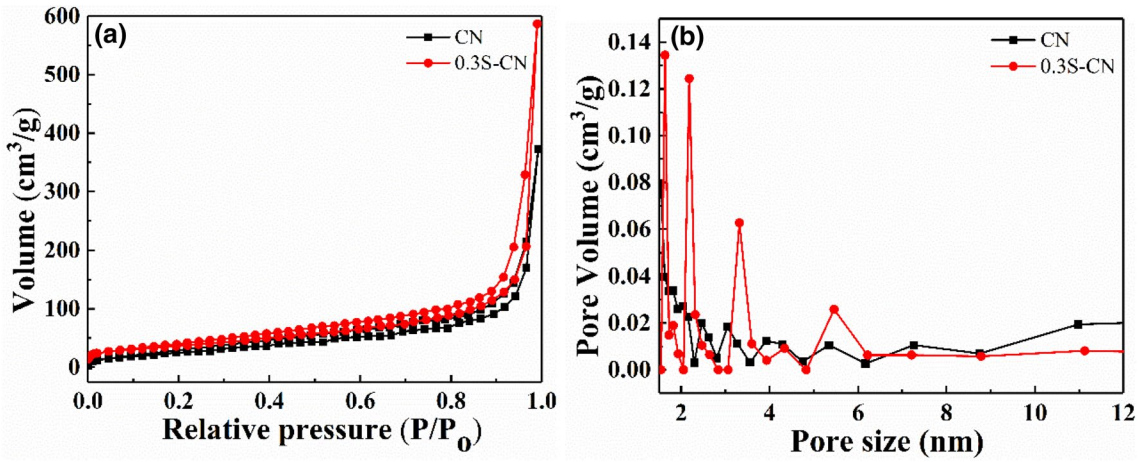

Fig. 3 N_2 adsorption–desorption isotherms and the corresponding pore size distribution curves of CN and 0.3S-CN

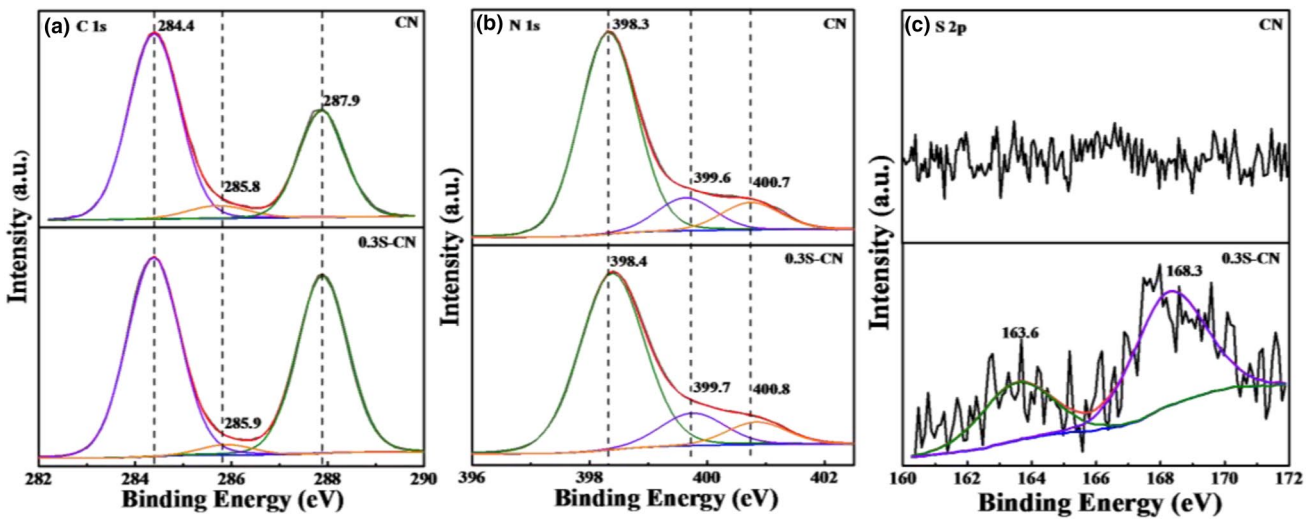

Fig. 4 XPS high resolution spectra for C1s (**a**), N1s (**b**) and S2p (**c**) of CN and 0.3S-CN

carbon impurities, respectively [15]. The N1s spectra in Fig. 4b can be mainly decomposed to three typical peaks located at about 398.4 eV, 399.7 eV, and 400.8 eV, which could be attributed to the sp^2-hybridized aromatic N atoms bonded to carbon atoms (C–N=C), and sp^3-hybridized N atoms of $N(–C)_3$ and terminal amino functions ($C–NH_x$), respectively [18, 19]. Table 1 showed the different component ratios of N1s spectra for CN and 0.3S-CN, in which the percentage of $C–H_X$ remains almost the same value, meaning the degree of polymerization is unchanged. The ration of N atoms in the sp^2-hybridized aromatic N atoms bonded to carbon (C–N=C) decreases to 75.5% from 77.1% of CN. The C/N ratio for CN and 0.3S-CN is close to the stoichiometric ratio of g-C_3N_4 by deducting the component of carbon impurities. These results demonstrated that these nanotubes are with carbon-rich structure. The S 2p peaks of the sulfur doped sample in Fig. 4c are centered at 163.6 eV and 168.3 eV. The peak at binding energy of 163.6 eV can be attributed to the formation of C–S in g-C_3N_4, indicating that S substitutes N atom [40, 41]. While the peak at binding energy of 168.3 eV can be attributed to the formation of S=O by oxygen adsorbed on the surface of 2-thiobarbituric acid during annealing process [42]. The results show that sulfur successfully enters the lattice of g-C_3N_4 and the formation of C–S bond in the framework of C–N bond.

Figure 5a shows the UV–vis diffuse reflectance spectra of g-C_3N_4 and S-doped g-C_3N_4. The maximum cut-off wavelength of pure g-C_3N_4 is 460 nm, and its band gap value is about 2.70 eV, which is related to the photocatalytic performance under visible light. The absorption intensity is significantly enhanced after S doping g-C_3N_4, and the maximum cut-off absorption wavelength appears obvious red shift phenomenon (480–614 nm), and the enhancement of the absorption performance in the visible light part can enhance the absorption performance (480–614 nm) [43, 44]. Insect in Fig. 5a shows the Kubelka–Munk function curves of pure g-C_3N_4 and S doped g-C_3N_4. After doping g-C_3N_4 with different amount of 2-thiobarbituric acid, the absorption intensity in visible light region is also significantly enhanced, and the band gap value gradually decreases to 2.67 eV, 2.66 eV, 2.57 eV and 2.29 eV for 0.05S-CN, 0.1S-CN, 0.3S-CN, 0.5S-CN and 1S-CN, respectively, compared to 2.70 eV of pure g-C_3N_4. The enhanced visible light absorption and relative narrow band gap energy may be attributed to the doping effect of S and C, which enables effective use of visible light.

Table 1 The component ratios of the N1s spectra for CN and 0.3S-CN

Samples	Binding energy (eV)	Peak assignment	Atomic percentage
CN	398.4	C–N=C (sp^2)	77.1
	399.7	N– $[C]_3$ (sp^3)	12.6
	400.8	$C–NH_X$	10.3
0.3S-CN	398.4	C–N=C (sp^2)	75.5
	399.7	N–$[C]_3$ (sp^3)	14.5
	400.8	$C–NH_X$	10.0

Figure 5b shows the transient photocurrent response curve of all sample electrodes, but under the same bias, the photocurrent of S-doped sample electrode is stronger than that of CN electrode, especially the photocurrent value of 0.3S-CN electrode is the highest, about 2.2 times of the photocurrent density of pure CN. The results show that the S-doped g-C_3N_4sample can form more photogenerated electrons and be effectively guided by light. It is shown in the figure that the transient photocurrent of S-doped g-C_3N_4 electrode can respond continuously, and there is no obvious decrease after 20 cycles, which shows that the structure of S-doped g-C_3N_4 sample is stable and there is no photo corrosion phenomenon. Figure 5c shows the impedance spectrum of g-C_3N_4 and S-doped g-C_3N_4 samples. The arc radius on the EIS indicates the charge transfer resistance [45, 46]. Generally, a smaller arc radius means a lower charge transfer resistance. The radius of EIS of S-doped g-C_3N_4 sample is obviously smaller than that of pure g-C_3N_4 sample, and the radius of EIS of 0.3S-CN sample reaches the minimum, which shows that the interface charge transfer resistance of the electrode obtained by S-doped g-C_3N_4 is smaller, which can effectively promote the transport and separation of photocarriers in catalytic reaction [21, 47, 48]. In addition, the change trend of EIS arc radius of g-C_3N_4 sample is basically consistent with that of PL spectrum, which is very important.

The photoluminescence (PL) spectra were carried out to investigate the recombination and separation of photoinduced charge carriers in the bulk g-C_3N_4, and the g-C_3N_4microwires under the excitation wavelength of 374 nm. The measured PL spectra, as shown in Fig. 5d, showed that all of the samples exhibit a main emission peak appearing at about 440 nm, which is consistent with the reported value in the literatures [41]. The PL intensity decreases after S doping, and 0.3S-CN exhibits lowest intensity, compared to the bulk g-C_3N_4. The weaker PL intensity revealing the lower recombination probability of photoinduced electrons and holes, which could give rise to a higher photocatalytic activity.

Figure 6a shows the Mott-Schottky plots with Ag/AgCl as reference electrode. The fitting slopes of g-$C_3N_4$and 0.3S-CN are positive, indicating that g-C_3N_4 and 0.3S-CN are n-type semiconductors. The flat band potential of g-C_3N_4 is − 0.94 V, which corresponds to the conduction band of − 0.94 eV, while that of 0.3S-CN is − 1.06 V, which corresponds to the conduction band of − 1.06 eV. As shown in Fig. 4a, the band gap value of g-C_3N_4 and 0.3S-CN is 2.70 eV and 2.57 eV, respectively. The valence bands are 1.76 eV and 1.51 eV, for CN and 0.3S-CN, respectively.

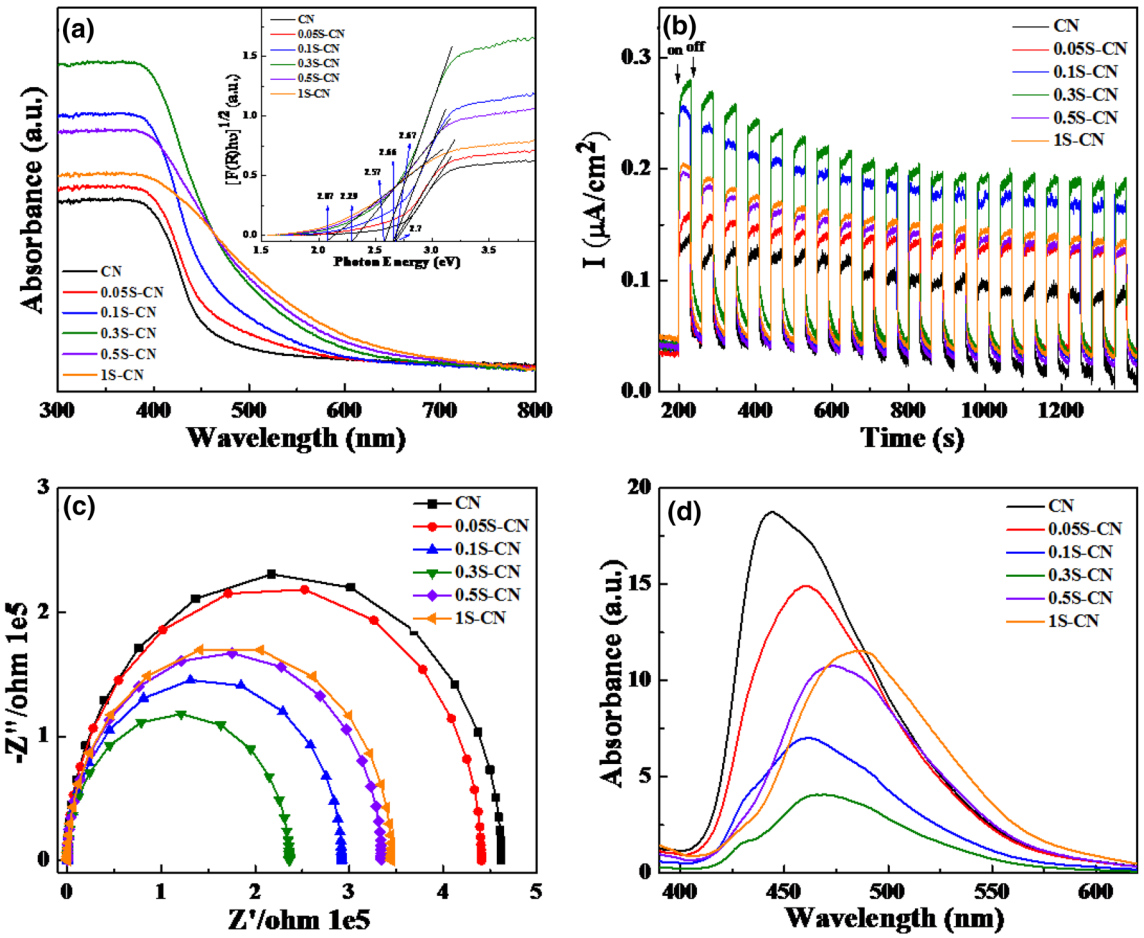

Fig. 5 UV–vis absorbance (**a**), transient photocurrent response (**b**), EIS (**c**), and PL spectra (**d**) of CN, 0.05S-CN, 0.1S-CN, 0.3S-CN, 0.5S-CN, and 1S-CN

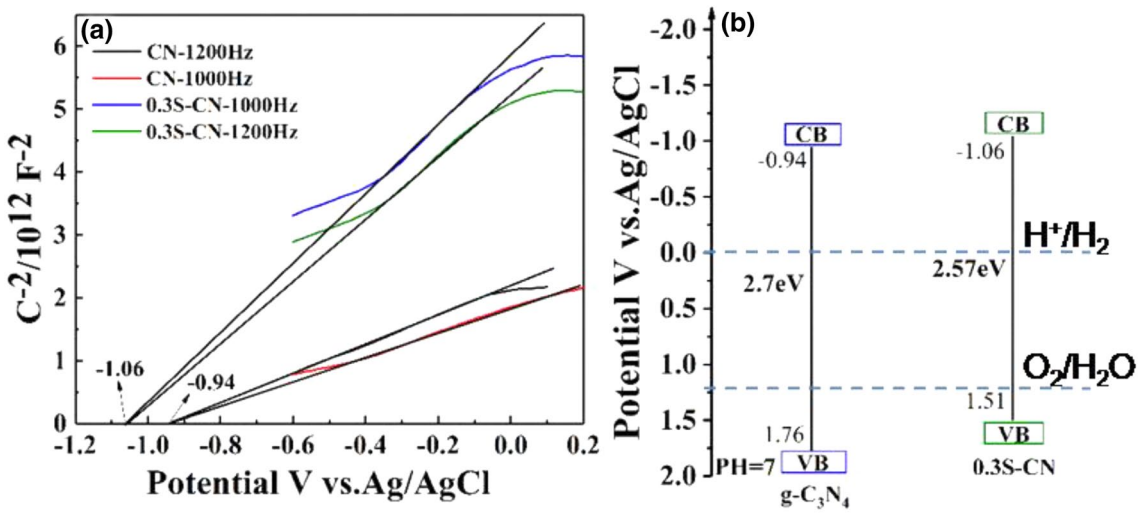

Fig. 6 Mott–Schottky plots (**a**) and proposed energy band diagram (**b**) of CN, and 0.3S-CN

Figure 6b shows the energy band structure of CN and 0.3S-CN. The reduction potential of 0.3S-CN is more negative than that of g-C_3N_4, which is an important reason why the photocatalytic efficiency of 0.3S-CN is higher than that of g-C_3N_4.

The photocatalytic performance of pure g-C_3N_4 and S-doped g-C_3N_4catalysts was characterized by photocatalytic hydrogen evolution under visible light irradiation ($\lambda > 420$ nm). 10 mg photocatalyst was dispersed in a solution containing 17 vol% TEOA and 3 wt% Pt ions. As shown in Fig. 7a, the photocatalytic H_2evolution is about 1.69 μmol/h, 2.35 μmol/h, 8.35 μmol/h, 9.52 μmol/h, 6.67 μmol/h and 2.90 μmol/h, for CN, 0.05S-CN 0.1S-CN, 0.3S-CN, 0.5S-CN and 1S-CN, respectively. After S doping, the hydrogen evolution performance of the catalysts is higher than that of pure CN, and the 0.3S-CN catalyst exhibits the best performance, which is about 5.85 times as high as that of pure g-C_3N_4. The photocatalytic performance of H_2 evolution of 0.3S-CN is better than or comparable to reported results [15, 16]. The stability of hydrogen evolution of 0.3S-CN catalyst was shown in Fig. 7b. After 5 cycles of photocatalytic hydrogen production, the activity of the sample did not decrease significantly, indicating that the catalyst can be recycled continuously, meeting the requirements of environmental protection. Table 2 presented the relationship between AQY and the crystallinity of S doped g-C_3N_4 nanotubes. The hydrogen evolution rate (HER) and AQY increase as the crystallinity increases. Considering XRD along with XPS results, we can deduce that HER improvement is resulted from the higher degree of crystallinity. S doping tunes the energy band structure, facilitating the transfer of photoinduced carrier charges.

Table 2 Correlation between the AQY (%) and the crystallinity of S doped g-C_3N_4

Samples	2θ position (°)	Crystallinity (%)	H_2 evolution rate (μmol/h)	AQY(%)
CN	27.25	23.2	1.69	0.96
0.05S-CN	27.35	19.5	2.35	1.33
0.1S-CN	27.35	20.3	8.35	4.73
0.3S-CN	27.32	22.0	9.53	5.39
0.5S-CN	27.25	20.5	6.67	3.78
1S-CN	27.25	12.5	2.90	1.65

XPS results showed that C and S were doped in the g-C_3N_4 framework, and C and S doping could induce the delocalized π bonds to increase the visible light absorption [15, 16]. UV–vis spectra showed the visible light harvesting increased after S and C doping. The enhanced visible light absorption and relative narrow band gap energy may be attributed to the doping effect of S and C, which enables effective use of visible light. EIS and PL results showed that S and C doping effectively promoted the transport and separation of photocarriers in catalytic reaction. The reduction potential of 0.3S-CN is more negative than that of g-C_3N_4, and this shift would increase the photoreduction ability of 0.3S-CN, compared with g-C_3N_4. Thus C and S doping enhances the hydrogen evolution ability of the catalyst under visible light.

4 Conclusion

In summary, the S-doped g-C_3N_4 photocatalyst was successfully prepared by the thermal polycondensation of 2-thiobarbituric acid and urea as precursor. Under the condition

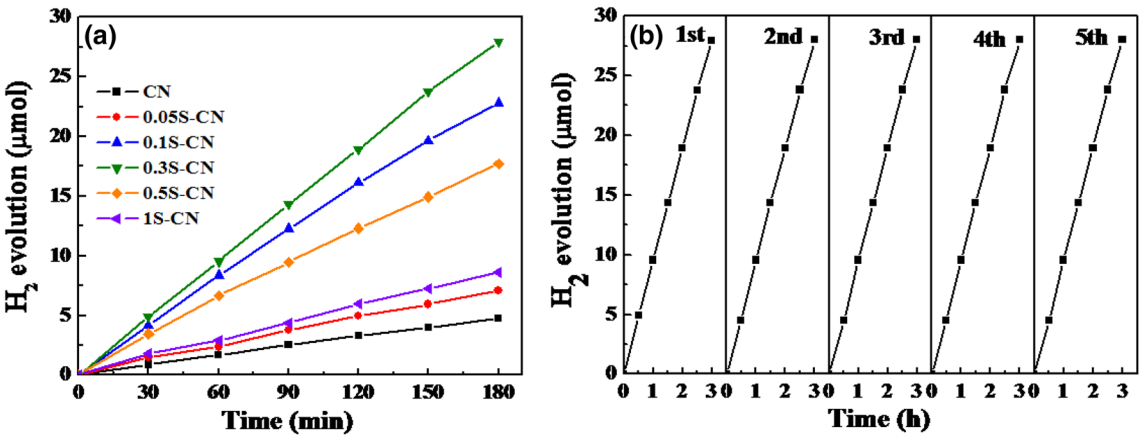

Fig. 7 Hydrogen evolution rates (**a**) of all sample and stability study (**b**) of photocatalytic H_2 evolution of 0.3S-CN under solar radiation with wavelength of $\lambda > 420$ nm

of visible light ($\lambda > 420$ nm), the photocatalytic activity was improved by introducing a small amount of 2-thiobarbituric acid into the g-C_3N_4 framework. The highest photocatalytic hydrogen evolution rate of 0.3S-CN is 9.3 μmol/h, which is 5.85 times that of g-C_3N_4. The experimental results show that S doped carbon rich g-C_3N_4 by 2-thiobarbituric acid as sulfur source can effectively reduce the band gap, tune the electronic structure of g-C_3N_4, and induces the reduction potential more negative, thus enhancing the hydrogen evolution ability of the catalyst under visible light.

Acknowledgments This work was financially supported by National Natural Science Foundation of China (51801164), Fundamental Research Funds for Central Universities (XDJK2020C005), Venture & Innovation Support Program for Chongqing Overseas Returnees (cx2018080).

Author Contributions The manuscript was written through contributions of all authors. All authors have given approval to the final version of the manuscript.

Compliance with Ethical Standards

Conflict of interest There are no conflicts of interest to declare.

References

1. Goettmann F, Thomas A, Antonietti M (2007) Metal-free activation CO_2 by mesoporous graphitic carbon nitride. Angew Chem Int Edit 46:2717–2720
2. Goettmann F, Fischer A, Antonietti M, Thomas A (2006) Chemical synthesis of mesoporous carbon nitrides using hard templates and their use as a metal-free catalyst for friedel-crafts reaction of benzene. Angew Chem Int Edit 45:4467–4471
3. Ruan LW, Qiu LG, Zhu YJ, Lu YX (2014) Analysis of electrical and optical properties of g-C_3N_4 with carbon-position doping. Acta Phys-Chim Sin 30:43–52
4. Guo LT, Cai YY, Ge JM, Zhang YN, Gong LH, Li XH, Wang KX, Ren QZ, Su J, Chen JS (2015) Multifunctional Au-Co@CN nanocatalyst for highly efficient hydrolysis of ammonia borane. ACS Catal 5:388–392
5. Datta KKR, Reddy BVS, Ariga K, Vinu A (2010) Gold nanoparticles embedded in a mesoporous carbon nitride stabilizer for highly efficient three-component coupling reaction. Angew Chem Int Edit 49:5961–5965
6. Li XH, Wang XC, Antonietti M (2012) Mesoporous g-C_3N_4 nanorods as multifunctional supports of ultrafine metal nanoparticles: hydrogen generation from water and reduction of nitrophenol with tandem catalysis in one step. Chem Sci 3:2170–2174
7. Zhu YP, Ren TZ, Ma TY, Yuan ZY (2014) Hierarchical structures from inorganic nanocrystal self-assembly for photoenergy utilization. Int J Photoenergy 3:1256–1271
8. Akbayrak S, Ozkar S (2012) Ruthenium(0) nanoparticles supported on multiwalled carbon nanotube as highly active catalyst for hydrogen generation from ammonia-borane. ACS Appl Mater Interfaces 4:6302–6310
9. Wang XC, Maeda K, Thomas A, Takanabe K, Xin G, Carlsson JM, Domen K, Antonietti M (2009) A metal-free polymeric photocatalyst for hydrogen production from water under visible light. Nat Mater 8:76–80
10. Zheng HR, Zhang JS, Wang XC, Fu XZ (2012) Modification of carbon nitride photocatalysts by copolymerization with diaminomaleonitrile. Acta Phys-Chim Sin 28:2336–2342
11. Zuluaga S, Liu LH, Shafiq N, Rupich SM, Veyan JF, Chabal YJ, Thonhauser T (2015) Structural band-gap tuning in g-C_3N_4. Phys Chem Chem Phys 17:957–962
12. Wang H, Yuan XZ, Wang H, Chen XH, Wu ZB, Jiang LB, Xiong WP, Zhang YX, Zeng GM (2015) One-step calcination method for synthesis of mesoporous g-C_3N_4/$NiTiO_3$ heterostructure photocatalyst with improved visible light photoactivity. RSC Adv 5:95643–95648
13. Stolbov S, Zuluaga S (2013) Sulfur doping effects on the electronic and geometric structures of graphitic carbon nitride photocatalyst: insights from first principles. J Phys-Condens Mat 25:7
14. Zhou YJ, Zhang LX, Liu JJ, Fan XQ, Wang BZ, Wang M, Ren WC, Wang J, Li ML, Shi JL (2015) Brand new P-doped g-C_3N_4: enhanced photocatalytic activity for H_2 evolution and Rhodamine B degradation under visible light. J Mater Chem A 3:3862–3867
15. Cao SH, Fan B, Feng YC, Chen H, Jiang F, Wang X (2018) Sulfur-doped g-C_3N_4 nanosheets with carbon vacancies: general synthesis and improved activity for simulated solar-light photocatalytic nitrogen fixation. Chem Eng J 353:147–156
16. Dong GH, Zhao K, Zhang LZ (2012) Carbon self-doping induced high electronic conductivity and photoreactivity of g-C_3N_4. Chem Commun 48:6178–6180
17. Yan SC, Li ZS, Zou ZG (2010) Photodegradation of rhodamine B and methyl orange over boron-doped g-C_3N_4 under visible light irradiation. Langmuir 26:3894–3901
18. Shi L, Liang L, Wang FX, Liu MS, Zhong SF, Sun JM (2015) Tetraethylorthosilicate induced preparation of mesoporous graphitic carbon nitride with improved visible light photocatalytic activity. Catal Commun 59:131–135
19. Lin QY, Li L, Liang SJ, Liu MH, Bi JH, Wu L (2015) Efficient synthesis of monolayer carbon nitride 2D nanosheet with tunable concentration and enhanced visible-light photocatalytic activities. Appl Catal B 163:135–142
20. Li J, Cheng SS, Du TX, Shang NZ, Gao ST, Feng C, Wang C, Wang Z (2018) Pd anchored on C_3N_4 nanosheets/reduced graphene oxide: an efficient catalyst for the transfer hydrogenation of alkenes. New J Chem 42:9324–9331
21. Dou HL, Long D, Zheng SH, Zhang YP (2018) A facile approach to synthesize graphitic carbon nitride microwires for enhanced photocatalytic H_2 evolution from water splitting under full solar spectrum. Catal Sci Technol 8:3599–3609
22. Liu Y, Yuan XZ, Wang H, Chen XH, Gu SS, Jiang Q, Wu ZB, Jiang LB, Wu Y, Zeng GM (2015) Novel visible light-induced g-C_3N_4-Sb_2S_3/$Sb_4O_5Cl_2$ composite photocatalysts for efficient degradation of methyl orange. Catal Commun 70:17–20
23. Wang JJ, Tang L, Zeng GM, Liu YN, Zhou YY, Deng YC, Wang JJ, Peng B (2017) Plasmonic Bi metal deposition and g-C_3N_4 coating on Bi_2WO_6 microspheres for efficient visible-light photocatalysis. ACS Sustainable Chem Eng 5:1062–1072
24. Munoz-Batista MJ, Fontelles-Carceller O, Ferrer M, Fernandez-Garcia M, Kubacka A (2016) Disinfection capability of Ag/g-C_3N_4 composite photocatalysts under UV and visible light illumination. Appl Catal B 183:86–95
25. Majeed I, Manzoor U, Kanodarwala FK, Nadeem MA, Hussain E, Ali H, Badshah A, Stride JA, Nadeem MA (2018) Pd-Ag decorated g-C_3N_4 as an efficient photocatalyst for hydrogen production from water under direct solar light irradiation. Catal Sci Technol 8:1183–1193

26. Dou HL, Zheng SH, Zhang YP (2018) The effect of metallic Fe(II) and nonmetallic S codoping on the photocatalytic performance of graphitic carbon nitride. RSC Adv 8:7558–7568
27. Yang Y, Zhang C, Huang D, Zeng G, Huang J, Lai C, Zhou C, Wang W, Guo H, Xue W, Deng R, Cheng M, Xiong W (2019) Boron nitride quantum dots decorated ultrathin porous g-C_3N_4: Intensified exciton dissociation and charge transfer for promoting visible-light-driven molecular oxygen activation. Appl Catal B Environ 245:87–99
28. Li JQ, Yuan H, Zhu ZF (2016) Improved photoelectrochemical performance of Z-scheme g-C_3N_4/Bi_2O_3/$BiPO_4$ heterostructure and degradation property. Appl Surf Sci 385:34–41
29. Zhou L, Zhang W, Chen L, Deng HP (2017) Z-scheme mechanism of photogenerated carriers for hybrid photocatalyst Ag_3PO_4/g-C_3N_4 in degradation of sulfamethoxazole. J Colloid Interface Sci 487:410–417
30. Yu S, Yun HJ, Kim YH, Yi J (2014) Carbon-doped TiO_2 nanoparticles wrapped with nanographene as a high performance photocatalyst for phenol degradation under visible light irradiation. Appl Catal B 144:893–899
31. Zhu YP, Ren TZ, Yuana ZY (2015) Mesoporous phosphorus-doped g-C_3N_4 nanostructured flowers with superior photocatalytic hydrogen evolution performance. ACS Appl Mater Interfaces 7:16850–16856
32. Zhang YJ, Mori T, Ye JH, Antonietti M (2010) Phosphorus-doped carbon nitride solid: enhanced electrical conductivity and photocurrent generation. J Am Chem Soc 132:6294–6300
33. Zhang LG, Chen XF, Guan J, Jiang YJ, Hou TG, Mu XD (2013) Facile synthesis of phosphorus doped graphitic carbon nitride polymers with enhanced visible-light photocatalytic activity. Mater Res Bull 48:3485–3491
34. Wang Y, Di Y, Antonietti M, Li HR, Chen XF, Wang XC (2010) Excellent visible-light photocatalysis of fluorinated polymeric carbon nitride solids. Chem Mater 22:5119–5121
35. Zhang Y, Antonietti M (2010) Photocurrent generation by polymeric carbon nitride solids: an initial step towards a novel photovoltaic system. Chem Asian J 5:1307–1311
36. Liu G, Niu P, Sun CH, Smith SC, Chen ZG, Lu GQ, Cheng HM (2010) Unique electronic structure induced high photoreactivity of sulfur-doped graphitic C_3N_4. J Am Chem Soc 132:11642–11648
37. Zhang JS, Sun JH, Maeda K, Domen K, Liu P, Antonietti M, Fu XZ, Wang XC (2011) Sulfur-mediated synthesis of carbon nitride: band-gap engineering and improved functions for photocatalysis. Energy Environ Sci 4:675–678
38. Hong JD, Xia XY, Wang YS, Xu R (2012) Mesoporous carbon nitride with in situ sulfur doping for enhanced photocatalytic hydrogen evolution from water under visible light. J Mater Chem 22:15006–15012
39. Li X, Qu Y, Wang G (2018) One-dimensional carbon self-doping g-C_3N_4 nanotubes: synthesis and application in dye-sensitized solar cells. Nano Res 11:1322–1330
40. Wang K, Li Q, Liu BS, Cheng B, Ho WK, Yu JG (2015) Sulfur-doped g-C_3N_4 with enhanced photocatalytic CO_2-reduction performance. Appl Catal B 176:44–52
41. Hamrin K, Johansson G, Fahlman A, Nordling C, Siegbahn K, Lindberg B (1968) Structure studies of sulphur compounds by ESCA. Chem Phys Lett 1:557–559
42. Chang YQ, Hong F, He CX, Zhang QL, Liu JH (2013) Nitrogen and sulfur dual-doped non-noble catalyst using fluidic acrylonitrile telomer as precursor for efficient oxygen reduction. Adv Mater 25:4794–4799
43. Ong WJ, Tan LL, Ng YH, Yong ST, Chai SP (2016) Graphitic carbon nitride (g-C_3N_4)-based photocatalysts for artificial photosynthesis and environmental remediation: are we a step closer to achieving sustainability? Chem Rev 116:7159–7329
44. Wang JP, Xu H, Qian XF, Dong YY, Gao JK, Qian GD, Yao JM (2015) Direct synthesis of porous nanorod-type graphitic carbon nitride/CuO composite from Cu-melamine supramolecular framework towards enhanced photocatalytic performance. Chem Asian J 10:1276–1280
45. Kumar S, Baruah A, Tonda S, Kumar B, Shanker V, Sreedhar B (2014) Cost-effective and eco-friendly synthesis of novel and stable N-doped ZnO/g-C_3N_4 core-shell nanoplates with excellent visible-light responsive photocatalysis. Nanoscale 6:4830–4842
46. Dou HL, Zheng SH, Zhang YP (2018) Graphitic carbon nitride with S and Fe(III) codoping for improved photodegradation performance. Catal Lett 148:601–611
47. Kong HJ, Won DH, Kim J, Woo SI (2016) Sulfur-doped g-C_3N_4/$BiVO_4$ composite photocatalyst for water oxidation under visible light. Chem Mater 28:1318–1324
48. Kou JH, Li ZS, Yuan YP, Zhang HT, Wang Y, Zou ZG (2009) Visible-light-induced photocatalytic oxidation of polycyclic aromatic hydrocarbons over tantalum oxynitride photocatalysts. Environ Sci Technol 43:2919–2924